CONTRIBUTION TO THE HOLLOW CYLINDER TEST ON THE STUDY OF ROCK FRACTURING THROUGH ACOUSTIC EMISSION MEASUREMENT

by João Miguel Mourato Vermelho Neves
Instituto Superior Técnico – Universidade de Lisboa

ABSTRACT

The present work aims to contribute to the development of the hollow cylinder test as a means to study the fracturing in rocks. For this purpose it was developed a methodology to record and locate the source of the acoustic emissions during the rock failure. The laboratory tests were also developed for this work, consisting on internally loading, leading to frank rupture, a triaxialy confined thick walled hollow cylinder. In order to locate the source of AE it has been developed an artificial neural network which was trained with artificial acoustic events using Hsu-Nielsen's Source. The trained neural network simulates the response time to the inverse location problem and is used as input in the resolution of the location of detected events. The AE location using this methodology shows good agreement with the visual analysis of specimens tested, and the error of the achieved location is near to that of the sensors.

This hollow cylinder test was also simulated with RFPA and the results are compared with the laboratory. Then both laboratory tests and RFPA's energy profiles were analyzed which allowed to draw conclusions on the importance of boundary conditions of the tests for effectiveness on the acurate location of detected events. It was also identified a characteristic energy signature for this hollow cylinder test.
.

KEYWORDS: Acoustic emissions, AE Source Location, Artificial Neural Networks, Hollow Cylinder Test, RFPA Simulation, Energy Profile Analysis.

INTRODUCTION

Europe is currently facing an environment of uncertainty about the future of its energy supply. After Fukushima, nuclear skeptical feelings abound almost everywhere within Europe(World Nuclear Association, 2014). The option to remove in the medium to long term, nuclear energy from the European energy mix, entails as an immediate consequence an increase of the weight of the other components in the equation of energy supply (WETTMANN, 2011). Namely added dependence of hydrocarbons, either coal or gas, thus increasing the energy dependency relative to the outer Europe (WETTMANN, 2011). This option conflicts with the energy independence goals set in the Europe 2020 strategy(European Commission, 2011).

The advent of shale gas in the middle of the last decade has enabled a radical change in the energy mix of the United States of America, (USA)(Melikoglu, 2014). Thanks to significant advances in horizontal and directed drilling techniques, as well as in hydraulic fracturing techniques (HF) it became commercially viable to exploit the gas trapped in the source rock. This, combined with the huge reserves found in the Marcellus, Haynesville and Barnett basins (US Energy Information Administration, 2011), contributed decisively to the United States' passing from the world's largest importer of hydrocarbons to exporter.

However, there are constraints to the exploitation of this resource, namely of environmental nature. As mentioned above, the exploitation of this resource is based on the recovery of the gas contained in the shale formations, which by nature have very low permeability. Thus, what in fact allows its exploitation is the use of HF treatments in the production borehole. These treatments aim to open fractures into the rock mass, thereby increasing the surface exposed to the borehole so that it contacts with the largest possible amount of source rock and therefore increasing production. Some of the issues related to the use of this technique are: uncertainties regarding the geomechanical stability of surrounding rock formations, as it is promoted its fracturing; Possible contamination of overlying aquifers above the shale formations; Leakage of greenhouse gases (CO_2, CH_4) into the atmosphere; Possible contamination of the soil, with consequences for the fauna, flora and human health.

It is not always possible to survey the whole risk, whereby a more detailed design of methods employed is essential. For this reason, many researchers are studying in detail how the fracturing process develops when using HF techniques, and means to establish models to predict the path and extent of the originated fractures (King, 2012). There are also inefficiencies in terms of propagation of fractures in pre-fractured sedimentary structures and phenomena of skewed fracture direction.

Solving these problems requires a better understanding of rock failure mechanisms and progression of fracturing, which also involves the investigation of the change of the stress state in the vicinity of the borehole.

As a triaxial test, the hollow cylinder test, hereinafter referred to as ECO, allows us to study these phenomena in a simplified manner. When prompted to rupture by an internal radial pressure, the tensile specimen breaks, which allows, in part, studying the shape of the rupture of the walls of a borehole in the HF treatments. Additionally, this test may be carried out by making a few adaptations to Hoek's triaxial cell, making it inexpensive and relatively easy to perform.

To enable such a study, it is nevertheless necessary to capture and record the propagation of fractures. This may be accomplished through the study and localization

of acoustic emission (AE), captured via a set of transducers.

The capture and localization of acoustic emissions in hollow cylinders for this type of study presents several problems. Problems which range from the absence of an agreed method for data interpretation, through the large amount of resources needed, to complex geometry that prevents direct wave propagation. For this reason, this work focus will be primarily on solving this problem. That is, to develop a methodology that allows the localization of the origin of the acoustic emissions while dealing with geometric constraints of the ECO and with the available equipment.

CAPTURE AND RECORDING OF AE IN LABORATORY

There are two types of the AE recording systems, one based on continuous wave signal where the sensors captures the entire profile of the elastic wave and where the registration is referred to as an acoustic signal; another, based on a discrete register referred to as an acoustic event. In both cases, the elastic wave is captured by piezoelectric transducers and converted into an electrical signal. The character of the frequency of an AE observed event depends mainly on the characteristics of the source and the distance between it and the sensor. In field studies have already been registered frequencies below 1 Hz; however, in laboratory studies phenomena typically have frequencies ranging up to 105 Hz (Hardy, 2005).

With regard to the interpretation of frequencies it is important to note that in most cases a single AE event has both components, P and S, and in some cases the distinction between them is not trivial (Hardy, 2005). It is also not uncommon to observe a third component due to surface waves; this is due to the fact that the transducer typically may be placed on a free surface of the material. This component is important since it is closely associated with the sensor resonance vibration. Consequently, the waveform of the AE and its parameters are not completely associated with the mechanisms of generation. But these are primarily responsible for any effect on the path between the source and the sensor having to be taken into account in selecting the material of the sensor. For example, it is important to consider the frequencies expected in the choice and design of the sensors. These have to be physically contained in the wave propagation zone of the sensor. In the case of the propagation zone is too short, to generate diffracted and dispersive waves (Grosse & Ohtsu, 2008), may induce significant errors in the subsequent data analysis.

AE SENSORS

An article by Mobley et al. (Mobley, 1987) describes the equipment necessary for registration of acoustic emission in laboratory studies. Hardy also in Laboratory monitoring systems, (Hardy, 2005), goes into considerable detail on the specifics and peculiarities of an AE recording systems. According to Hardy, AE events from laboratory experiments have the following characteristics that set them apart from events captured in fieldwork: Signal Frequencies predominantly in the range of high frequencies, typically in the hundreds of kHz; Signal of low amplitude; Cadence very high events; Remarkable complexity of the signal profile due to reflection of elastic waves at the borders of the specimen under test and its particular geometry.

According Hardy, these characteristics are major constraints as regards the design and choice of sensors used (Hardy, 2005).

Since the dimensions of laboratory specimens are typically limited to between a few cm and 2 m, the energy available for the majority of events is small, they have originated in inter or intra grain ruptures, fractures coalescence or spread of micro and macro fractures. It follows that the frequency of each event signal is high and of low amplitude. However, since the distance between the event source and the sensor is also small, the amplitude attenuation phenomena are also reduced, which ultimately produce a large number of events detected.

To the problem of the complexity of the specimen boundaries introducing reflections that can have both a constructive nature as destructive in elastic waves, Hardy adds the importance of heterogeneity in geological materials, which can generate refraction events and internal reflection, producing more complex patterns in sign. However, in this regard, Ohtsu states that the elastic-dynamic field of the material properties are fundamentally dependent on the characteristic dimension of their constituents, and it is considered reasonable to rock as a homogeneous material with regard to the noise measurements. Ohtsu justifies this with the disparity between the heterogeneity of the characteristic dimensions (grain size or micro pre-existing fractures) and the size of the AE wavelength, making any effect of heterogeneity of inconsequential material in the measurement of AE (Grosse & Ohtsu , 2008).

In complex specimens, typically sequences from different geological units as used in the simulation of complex reservoirs, the interface between structures must be taken into account, so that this simplification is not always possible.

There are many piezoelectric materials with appropriate properties for the manufacturing of piezoelectric sensors. Although there mono natural crystals such as gallium phosphate, quartz or tourmaline, piezoceramic elements are frequently used in most applications, because they provide greater durability and sensitivity. Common examples are barium titanate and lead zirconate titanate (Hardy, 2005). There are also mono synthetic crystals as exemplified magnesium niobate and lead - lead titanate (PMN-PT) that offers superior sensitivity of piezoceramic leagues. However they are also more sensitive to temperature, having a less accurate at very high temperatures, furthermost they are significantly more expensive.

For use in laboratory work there are essentially four types of piezoelectric transducers, respectively called accelerometers, AE transducers, piezoelectric elements, and semiconductor strain gauges (Hardy, 2005). In this work we are used AE transducers.

AE Source LocationThere are two commonly used approaches, the first based on the use of only a single triaxial seismometer station incorporating a transducer; the second, more predominantly used in both field and laboratory studies (Hardy, 2005), is based on the use of

a network composed of multiple transducers. The method used is the trajectory Times difference (Travel-time-difference, TTD) which refers the problem of location for the resolution of the equation 1 (Hardy, 2005):

$$(x_i - x_s)^2 + (y_i - y_s)^2 + (z_i - z_s)^2 = V_i^2(t_i - T_s)^2 \qquad [1]$$

Where x_i, y_i, z_i and t_i are respectively the known cartesian coordinates of the i-index sensor and time the event was logged in this sensor. The unknown components x_s, y_s, z_s and T_s are referring to the origin of acoustic emission. That said we have an equation with four unknowns, which implies that in order for the system solution to be exactly determined in space, it is necessary the information of four transducers. However, according to Hardy, there are inherent errors in the positioning of the sensors, determination of event registration time in the sensor and the seismic velocity of the acoustic wave in the medium. Therefore, at least five sensors should be used, forcing the solution of the system to be over determined (Hardy, 2005). This method assumes that the propagation medium is homogeneous, i.e. there are no heterogeneities that cause refraction of the waves by forcing them into complex pathways until arrival at the sensor. Another assumption is that there is a direct propagation path between the source of the elastic wave and the transducer. That is, the method assumes that the waves travel in a straight line from the origin to the sensor, which is not always true, particularly in rock specimens of heterogeneous nature. However, as mentioned above for the wavelengths associated with the acoustic emissions in laboratory scale inhomogeneities of the sample are rendered irrelevant, which allows them to be compared to a homogeneous medium. Furthermore, in the laboratory it is sometimes convenient to use specimens with complex geometries, such as the testing of hollow cylinders; this complex geometry of the sample borders makes it impossible, for there to be for some points, a continuous straight path between the source and the sensor.

The approach to the location where complex geometry was proposed by Ing et al. and Ribay et al. (Ing, Quieffin, Catheline, & Fink, 2005; Ribay et al., 2007) and requires the modelling of an artificial neural network or temporal inversion technique based on the response function to the elastic impulse.

According to Kundu, the method relies on constructing a training matrix that is obtained through a precise request specimen surface along a well-defined mesh points in space. The response function to the elastic pulse is recorded for each grid point on each of the sensors, thereby yielding a virtual model discriminated speeds for each specimen of the zones defined by the fabric for each of the sensors. When it causes an acoustic emission in the specimen that you want to find, you need to compare the event log for each sensor and compare with the response functions to push the mesh if choosing the one with the highest correlation with the training matrix (Kundu, 2014).

Similar approaches utilizing the reversal of the impulse response function avoiding the analysis of mechanical waves have been proposed by various authors (Grabec & Sachse, 1989; Kosel, Grabec, & Muzic, 2000; Sribar & Sachse, 1993). These authors use an artificial neural network and pattern recognition techniques in order to solve the inversion problem. The advantage of these techniques is that they do not require prior knowledge of the velocity of elastic waves or geometric contours of the surface of the specimen. (Kundu 2014). These techniques however are computationally demanding and require a lot of preparation work. The construction of the training matrix requires the repetition of tests on each grid point several times, which in large specimens can take a long time.

According to Kundo, this is the reason why Park et al. made a more expedite technique to automate the process of building the training matrix using for this purpose a laser scanning Doppler Vibrometer (SLDV) (Kundu, 2014), capable of measuring propagation velocities based on the principle of the Doppler effect (Scruby & Drain, 1990; Staszewski, Lee, Mallet, & Scarpa, 2004). In principle this technique enables the location of the source of acoustic emissions in any structure regardless of its geometric complexity (Park et al., 2012). However to date the complex structures in which the technique was tested is still limited (Kundu, 2014).

The problem of locating the source of acoustic emissions in specimens containing internal cavities of circular profile was addressed by Baxter et al. It is proposed a methodology called "Delta T" for the location of the events (Baxter, Pullin, Holford, & Evans, 2007). This method is based on a battery of artificially generated test events by Hsu-Nielsen pencil lead break test (Hsu, 1977). In each point of the test matrix are generated ten artificial events. The average of the ten times is recorded at each sensor for each point. Using linear interpolation between the points of the test matrix, builds up a map of the differences in expected time for each point of the specimen. Hensman et al. significantly improves this technique by introducing probabilistic interpretation, what reduces the amount of training events (Hensman, Mills, Pierce, Worden, & Eaton, 2010).

LABORATORIAL PROCEDURES

SENSOR VALIDATION AND MAX TIME CONTROL

After the purged of both hydraulic systems, the test pieces are subjected to a stress state whose confinement component is equal to the axial stress. They are then recorded sequentially (Table 1), the following travel time of an ultrasonic pulse from sensors:

1º	S1 – S2	2º	S2 – S1
3º	S2 – S3	4º	S3 – S2
5º	S3 – S4	6º	S4 – S3
7º	S4 – S2	8º	S2 – S4
9º	S1 – S4	10º	S4 – S1
11º	S1 – S3	12º	S3 – S1

Table 1 – Time test order for S_A-S_B and S_B-S_A.

These times are recorded for each specimen at all load levels, up to the level at which the specimen is tested. So whereas for the specimens tested at 1 MPa only these load times were recorded, for the tests at 3 MPa were recorded the load times to 1 MPa, 2 MPa and 3 MPa. The piezoelectric properties of the sensors allow the reception of an electrical impulse in the sensor, which is converted to a mechanical impulse, ie, acoustic wave. The acoustic wave is detected by another sensor, which transforms it back into electrical impulses. The travel time on the cables is negligible and thus the time between the instant when the electrical impulse is sent to the first sensor and the instant at which the electrical impulse arrives from the second sensor is considered the mechanical impulse travel time within the specimen.

As the Euclidean distances between each sensor are known this method allows us to determine the average linear velocity of the pulse within the sample between each pair of sensors. The "swapped" times, i.e., the time measured the same way with the sensors roles reversed are vital to control the stability and reliability of the sensors.

This measurement of travel times between sensors was recorded for each increment of the confinement tensions.

From the validated tests, four were tested with confinement stress equal to axial stress (1 MPa), ensuring that the failure was produced by the internal pressure introduced into the hose. The other four were tested at 2 MPa and four others were tested at 3 MPa. Thus were recorded twelve sets times for 1 MPa, eight sets to 2 MPa and four sets to 3 MPa.

These power levels are not random. If the pressure inside the oil pressure chamber exceeds 3.5 MPa, the resin proofing the openings where the sensors are yields, allowing the oil to contact the sample. The same is true for the holes where the sensor coaxial cables exit, though this critical pressure is slightly above 4 MPa. For this reason, it was imposed a limit of 3 MPa to the maximum confinement load, the other loads were defined as 1/2 and 1/3 of the maximum load, 2 MPa and 1 MPa respectively.

LOADING OF INTERNAL RADIAL PRESSURE UNTIL RUPTURE

After validated, the sensors are connected to preamplifiers thus completing the circuit data acquisition group. Using a metal rod, an artificially acoustic event is generated on the outer surface of the body of the Hoek's triaxial cell, to verify if the system is capable of recording the event (testing its sensitivity) and its stability. After confirming the sensitivity and stability of the system, it starts to increase the loading of the internal radial pressure. This loading is performed manually at a rate of approximately 0.7 MPa per second. The accumulated acoustic events are registered regarding the internal radial pressure.

The increasing of the internal radial pressure is interrupted when, simultaneously, there is a drastic increment of the events count coupled with a confinement pressure drop. Other clear indications of specimen failure are the audible characteristic sound of the rupture specimen and an oil spill from the lower plunger.

The sample is then unloaded, removed and photographed.

It is also recorded the number of events at the time of rupture, and subsequently occurred records to this are discarded because they are contaminated by noise injection of fluid into the fracture. Although it is certain that this procedure deletes part of the of failure AE it is also the only one that guarantees no contamination of data.

A summary of the results is shown in Table 3, where σ_{RADIAL} corresponds to the outer containment pressure, σ_{AXIAL} corresponds to axial stress confinement, σ_{IAE} corresponds to internal pressure for which it was recorded the first sound event and $\sigma_{RUPTURE}$ corresponds to internal pressure to which occurred the rupture of the specimens. Identification of the tested specimens is made with the PV prefix for specimen abbreviation, followed by two digits with the number identifying the order in which the specimens were tested. Assays of samples PV01, PV04, PV06, PV08, PV18, PV22, PV23 and PV33 are missing from the table because they were aborted trials and invalidated. The c suffix in PV34 test was added because it was necessary to mount it several times due to abnormal signals from the sensors.

Sample	σ_{AXIAL}	σ_{RADIAL}	σ_{IEA}	$\sigma_{RUPTURE}$	EA Total
PV02	3	3	14	14	267
PV03	2	2	16	17	600
PV05	3	3	4	24	681
PV07	3	3	24	27	1648
PV09	3	3	26	26	150
PV10	3	3	28	28	106
PV11	3	3	4	30	27
PV12	2	2	10	21	1021
PV13	2	2	28	28	690
PV14	2	2	7	24	721
PV15	2	2	13	24	932
PV16	2	2	3	23	399
PV17	1	1	17	20	869
PV19	1	1	10	22	1060
PV20	1	1	1	23	573
PV21	1	1	20	20	715
PV24	1	1	25	25	315
PV25	2	2	26	26	1343
PV26	3	3	4	29	919
PV27	1	1	1	28	1165
PV28	2	2	7	27	1182
PV29	1	1	14	25	1203
PV30	1	1	2	20	1171
PV31	2	2	13	26	1554
PV32	2	2	4	26	589
PV34c	3	3	1	29	2589
PV35	3	3	10	28	331
PV36	3	3	4	27	334
PV37	3	3	10	28	411
PV38	1	1	7	20	905
PV39	1	1	1	18	588
PV40	2	2	4	23	679

Table 2 – Summary of the performed ECO.

AE DATA TREATMENT

FILTERING THE ELECTROSTATIC NOISE

At the start of the tests, it was noted that there was an intermittent electrostatic noise, which made it impossible to collect data. It was opted for a threshold of 65 dB, testing prior to each test which was the noise threshold and rehearsing only whith a threshold below 65 dB.

PAIRING OF THE ACOUSTIC EVENTS

It was decided to create a time parameter that allowed to set limits to the difference in arrival times for each sensor for the same event. These times were the maximum times recorded for each pair of sensors during the validation of the sensors, so a difference of times higher than the presented below is impossible. Thus it was created 6 temporal conditions paired events must meet: $\Delta t_{(S1-S2)} \leq 9,9$ µs; $\Delta t_{(S1-S3)} \leq 15,4$ µs; $\Delta t_{(S1-S4)} \leq 15,2$ µs; $\Delta t_{(S2-S3)} \leq 14,9$ µs; $\Delta t_{(S2-S4)} \leq 15,9$ µs; $\Delta t_{(S3-S4)} \leq 9,8$ µs.

TRAINING MATRIX

To develop the training matrix were randomly chosen three specimens from among the specimens for testing, hereinafter referred to as PVT1, PVT2 and PVT3. In each of the specimens was printed on its surface a mesh, 15:24, of 360 points uniformly distributed over 15 lines perpendicular to the sample axis, with a minimum distance between adjacent dots of 5.5 mm. However, the diameter of sensors used was 15 mm so this definition of the mesh is too large. So there were numbered points only of the odd rows and columns, doubling the minimum spacing between adjacent points, getting a mesh 8:12 with 96 points. Four sensors so that for all samples the location of each sensor for all mesh points 8:12 equals were then coupled. Thus not only are known the coordinates of each point of the grid but also the center coordinates of each of the sensors.

The four sensors of response times are then tested for each of the matrix points. For this purpose, 10 test acoustic events are artificially generated in each point, using the source Hsu-Nielsen, pencil lead break (Hsu, 1977). The Hsu-Nielsen source consists in bending until breakage on the surface of the specimen, from one end of hardness H2 mine with length between 3 mm and 5 mm (Figure 1).
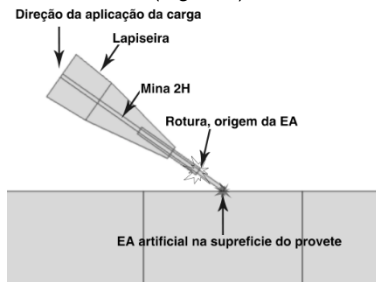
Figure 1 –Hsu-Nielsen's, adapted from (SAUSE, 2011).

After testing all 90 points in both samples, the information is organized in two arrays 900x7 in the form shown in equation 2:

$$Mteste_{cart} = \begin{bmatrix} \rho_1 \cos\theta_1 & \rho_1 \sin\theta_1 & z_1 & tS1_1 & tS2_1 & tS3_1 & tS4_1 \\ \vdots & \vdots & \vdots & \vdots & \vdots & \vdots & \vdots \\ \rho_{900}\cos\theta_{900} & \rho_{900}\sin\theta_{900} & z_{900} & tS1_{900} & tS2_{900} & tS3_{900} & tS4_{900} \end{bmatrix} \quad [2]$$

Subsequently the test matrix is divided into two arrays with the same index; PREINPUT the matrix and PRETARGET matrix equations 7:08 respectively:

$$PREINPUT = \begin{bmatrix} \rho_1\cos\theta_1 & \rho_1\sin\theta_1 & z_1 \\ \vdots & \vdots & \vdots \\ \rho_{900}\cos\theta_{900} & \rho_{900}\sin\theta_{900} & z_{900} \end{bmatrix} = \begin{bmatrix} x_1 & y_1 & z_1 \\ \vdots & \vdots & \vdots \\ x_{900} & y_{900} & z_{900} \end{bmatrix} \quad [3]$$

$$PRETARGET = \begin{bmatrix} tS1_1 & tS2_1 & tS3_1 & tS4_1 \\ \vdots & \vdots & \vdots & \vdots \\ tS1_{900} & tS2_{900} & tS3_{900} & tS4_{900} \end{bmatrix} \quad [4]$$

ARTIFICIAL NEURAL NETWORK

The direct approach is assumed as the input signal detection and output while the Cartesian coordinates of the origin of the acoustic event. That is, four inputs and three outputs, which complies with the principle of maintaining the higher number of input parameters or equal to the number of output parameters. However it is not possible to obtain satisfactory results with this approach regardless of the number of neurons in the hidden layer. Thus, reversing the approach chosen network architecture is represented by the graph 12: 24: 6. That is, as shown in the diagram of Figure 2 the network has twelve inputs, one hidden layer with twenty-four neurons, and a layer with six outputs.
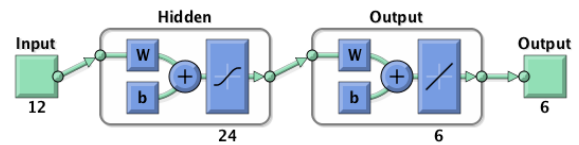

Figure 2 – ANN Diagram.

ANN TRAINING

The neural network created is a multilayer feedforward network with back propagation of error; training algorithm used was the Levenberg-Marquardt algorithm, hereinafter referred to as ALM. ALM was first described by (Marquardt, 1963), it is a widely used algorithm and numerous applications. Its application to the training of neural networks is described in (Martin T. Hagan & Menhaj, 1994) and (M T Hagan, Demuth, & Beale, 1996). The version used here is the algorithm included in MATLAB from MathWorks, Inc.

The group that feeds the input layer is a vector matrix C = 12xQ, where Q is the number of detected events. The output assembly is T = Qx6 vector array.

As shown in Table 3, the final performance of the network during training was satisfactory with low average squared errors and correspondence between the expected values and the approximate of around 93%. In addition there is the good performance of the network generalization capacity.

	No. Samples	EMQ	Correlation
Training	674	4,80	0,930
Validation	135	4,53	0,932
Test	90	5,29	0,929

Table 3 – ANN's Regression performance resume.

It is also noted, as evidenced by the distribution of the differences between the expected values and approximate in Figure 3, the majority of the patterns had a good approximation with more than 60% has an error lower than 2.5 ns.
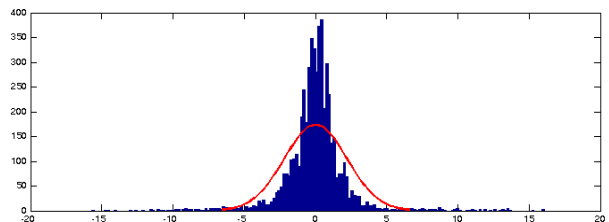

Figure 3 – ANN error distribution.

5

INVERSE LOCATION SOLVING

Consider the function $h: \mathbb{R}^{12} \rightarrow \mathbb{R}^6$ generated by the neural network and generically defined in equation 5:

$$h(c) = t', \qquad [5]$$

where $c \in \mathbb{R}^{12}$ e $t' \in \mathbb{R}^6$, as the function that simulates the difference between the time instants at which the acoustic event is detected at each sensor. Consider also the objective function $\varepsilon: \mathbb{R}^{18} \rightarrow \mathbb{R}$ defined by equation 6:

$$\varepsilon(c, T_j) = \sum_{i=1}^{6} (h_i(c) - T_{ji})^2, \qquad [6]$$

being T_j an input matrix defined in equation 19. One way to solve the inverse problem is to minimize ε, where the coordinates of the event source j, (C_j), are approximated by equation 7:

$$C_j \approx \widetilde{C_j} = \min_c \varepsilon(c, T_j), \qquad [7]$$

The solutions were constrained with the following conditions:

$$2{,}25^2 \leq x_i^2 + y_i^2 \leq 21^2 \qquad [8]$$

$$0 \geq z_i \geq -84 \qquad [9]$$

ACCURACY AND EFFECTIVENESS TEST

In order to ingest about the effectiveness and accuracy of the system of coordinates in each tested for the ability to locate events whose origin is already known. For this purpose we used the events recorded in the training matrix for the PVT1 specimen, and the neural network was trained with training events PVT2 specimen. The result of the location of the 900 tested events is shown in Figure 4 where you can see the good ability to locate events in the sample surface.
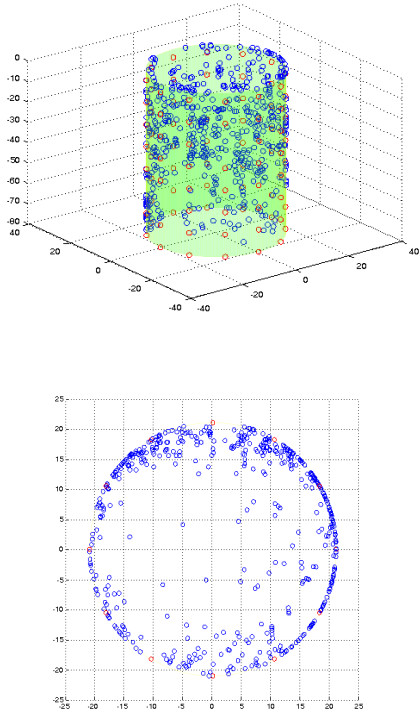
Figure 4 - PVT1 training events localized with PVT2's events trained ANN.

The location of the error is defined as the Euclidean distance between the known and located origin. The average error in the approximation of x, y and z are respectively 22.8 mm, 13.1 mm and 9.5 mm and the maximum forward error uncertainty associated with the sensors that have a diameter of 15 mm.

To represent and simulate the test RFPA2D, constituted by an array of 180 elements or nodes 84, each of which contains a set of mechanical parameters with a random distribution and dimensions 0.25 mm². The dimensions of the array and its elements reflect the fact that if you want to represent the heterogeneity of the grain scale, having this an approximate diameter of 0.5 mm. The mechanical parameters for each node are given by functions defined $f: \mathbb{R}^3 \rightarrow \mathbb{R}$, with Weibull distribution and the kind of writing in Equation 24:

$$f(x, \lambda, m) = \begin{cases} \frac{m}{\lambda}\left(\frac{x}{\lambda}\right)^{m-1} e^{-(x/\lambda)^m}, & x \geq 0 \\ 0, & x < 0 \end{cases} \qquad [10]$$

The matrix is composed by three distinct sets:

The first set is the tops and aims to simulate the behaviour of the steel pistons. For purposes of the simulation it was found that the steel piston is used in the AISI grade A514 B (AZO Materials, 2013). The mechanical properties, that software authors consider that are relevant for the simulation are: Compression resistance (σ_c) , of 760 MPa; Poisson's coefficient (ν), of 0,28; and Young's Modulus (E), of 210 GPa.

So these are the reference values to be assigned to the characteristic parameter λ. Since steel is a homogeneous material, the values for m have been arbitrated for the three equals 100, once for m = 100 the value of all nodes very close orbits around the characteristic value λ. The ratio T / C is defined as the ratio of the compressive strength by tensile strength, in the steel of 1.

The second set intends to simulate the bore of the hollow cylinder, hollow, whose properties do not depend on a distribution function and include the initial internal pressure and the pressure increase during the test, constant and always equal to 1 MPa by iterative cycle.

The last set is the simulation of the rock matrix. For this set the parameters in λ they were initially approached by heuristic criteria and honed by back analysis. After this process the parameters λ for σ_c, ν and E are 120 MPa, 0,27 and 82,4 GPa.

Values m vary depending on the value of the confinement stresses. For the simulation confinement stress of 1 MPa parameters m for σ_c, E e ν were respectively 2.9, 3.4 and 100. Considering therefore that the ratio between the deformation does not change with increasing confinement stresses and is constant throughout the specimen. To 2 MPa and 3 MPa parameters m for σ_c and E are 2.9, 2.8 e 3.6, 3.6.

RESULTS

EVENTS LOCALIZATION

All samples were photographed after the test and data from acoustic emissions after processing are designed in photographs. Thus it is possible to compare the position of the event located on the final fracture. Figures 5, 6 and 7 are representative examples of tests made with confinements of 1 MPa 2 MPa and 3 MPa respectively.

Figure 5 is an example of a location taken in a test with 1 MPa radial and axial confinement. It was possible to locate 156 of the 404 detected events. The total number of detected events is determined by the sensor that detects more events throughout the study. So in this case it is located about 38.6% of detected events.
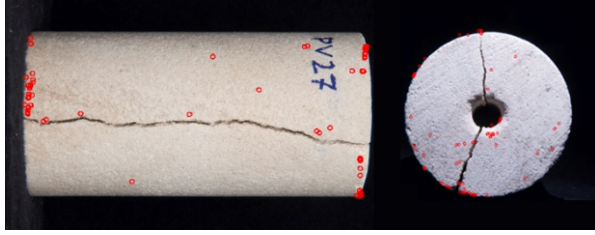
Figure 5 - Events located for 1 MPa confined PV27.

Figure 6 is an example of a location taken in a test with 2 MPa radial and axial confinements. It was possible to locate 211 of 373 detected events. Since the ratio of the events detected and localized been 56.6%.
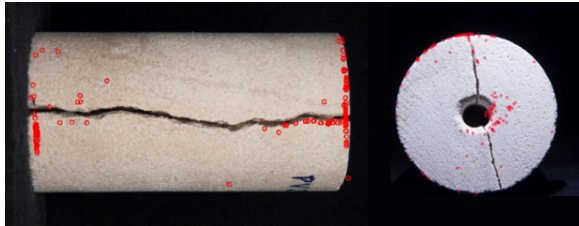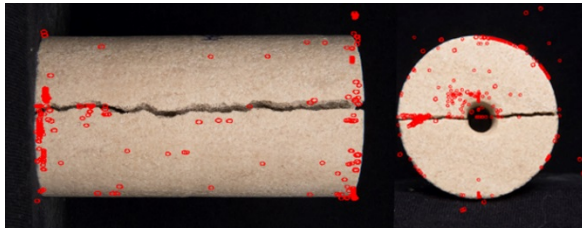

Figure 6 – Events located for 2 MPa confined PV28.

Figure 7 is an example of a location taken in a test with 3 MPa radial and axial confinement. It was possible to locate 484 of the 768 detected events. Since the ratio of the events detected and localized been 63.0%.

Figure 7 - Events located for 3 MPa confined PV34c.

Analysing the graph of Figure 8 it is noticed that this increase in the percentage of events is found widespread.
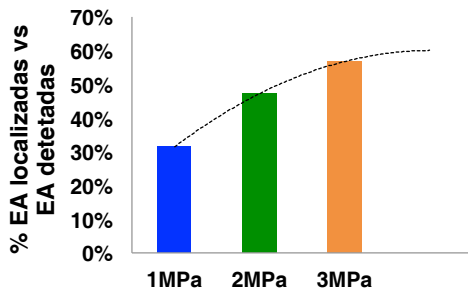
Figure 8 - % Located AE vs Detected AE.

Another interesting analysis is determined that the percentage of localized EA does not appear to depend on the rock matrix and the pre-existing micro-fracturing, as can be seen in Figure 9. The samples PV26, PV27, PV28 and PV 29 were taken from the same block, the same being true for the pair PV30, PV31, PV32 and PV35 and also to PV34c, PV36, PV37, PV38, PV39 and PV40. The PV25 specimen belongs to another series of specimens in which errors occurred during data acquisition.
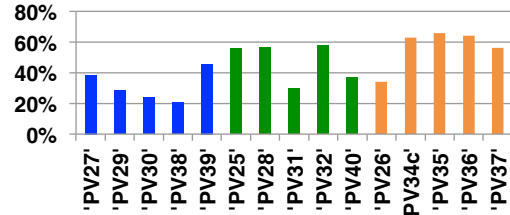
Figure 9 - % Located AE vs. Detected AE.

RFPA ECO SIMULATION

In order to visualize the progression of the emission EA is presented for each simulation 3 steps, 33%, 66% and 100% of the tensile strength respectively (as can be seen in Table 3). Figure 10 shows the simulation obtained for 1 MPa to 2 in Figure 11 and Figure 13 MPa to 3 MPa. The energy scale used in representing the AS changes, for each simulation, each iteration for this is provided below for each step, as shown in Figure 10. It was not possible to find any correlation between different simulations energy scales, although the unit energy is always the Joule, which makes the visual comparison between simulations.
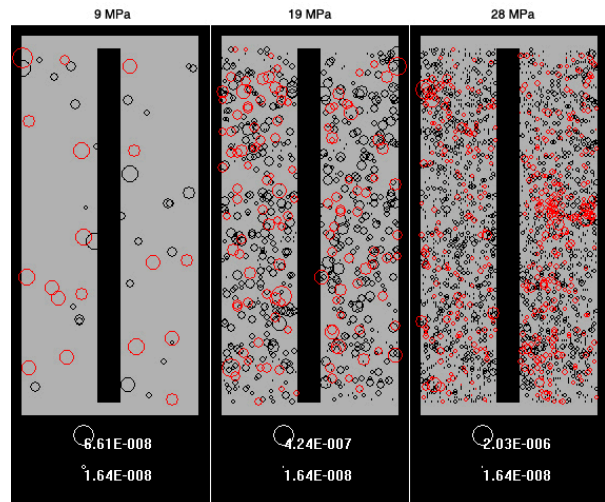

Figure 10 – RFPA simulation for 1 MPa confinemnet.

In fact, even getting in touch with the events of the trials, although detected were not traceable there is considerable discrepancy between the scale of the event count. At first sight it stands out more than the quality of the simulated emission quantity.
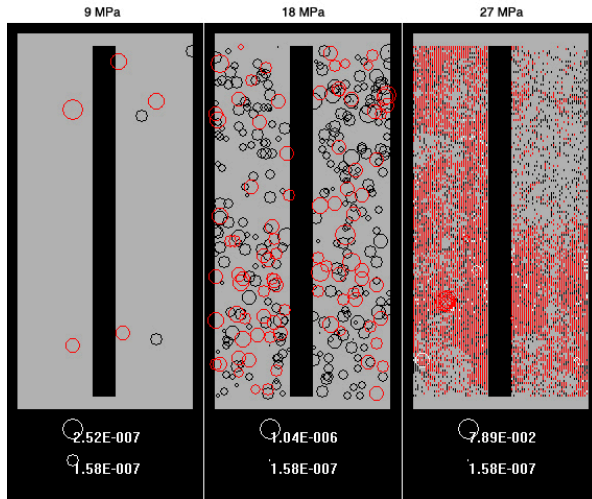
Figure 11 – RFPA simulation for 2 MPa confinment.

Figure 13 – RFPA simulation for 3 MPa confinemnet.

In this simulation it was possible to recreate the most common fracture profile between the tests. The total rupture of one side and the other only partially verified in most laboratory tests as shown in Figure 12. This phenomenon is noticeable due to injection of the fluid after breaking free when cut edges of the fracture pressure hose internal.

Figure 12 – Photographed after ECO of PV32 e PV34.

However this is not the general case. As part of this work were made in the total containment of the various conditions, more than two hundred RFPA simulations, however the number of simulations that produce rupture of profiles as in Figure 12 is less than 5% of the sample.

It is possible however to note that there is a clear differentiation between the energy level of simulations for different voltages confinement when it exceeds 2/3 of the breaking load value. The simulations for confining pressure to 1 MPa produced EA simulated whose maximum values for the energy is of the order of 10^{-6} J. For 2 MPa and 3 MPa These values are on the order of 10^{-2} J and 10^{-1} J, respectively, which is a considerable variation. For this reason we proceeded to the processing of data of the energies of laboratory tests.

RFPA SIMULATION ENERGETIC PROFILES

The graphs of Figures 14, 15 and 16 represent the energy profiles of the RFPA simulations with axial and radial confinement stress of 1 MPa 2 MPa and 3 MPa respectively.
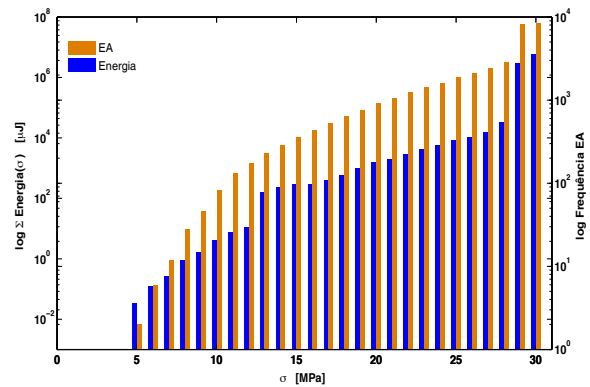
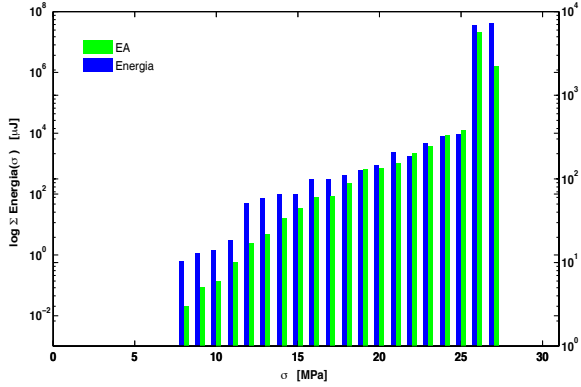

Figure 14 - 1 MPa RFPA2D energy profile.
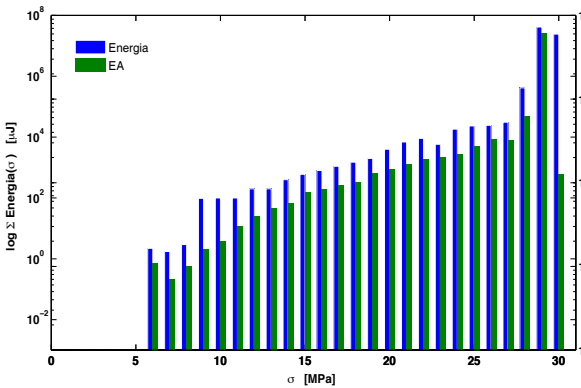
Figure 15 - 2 MPa RFPA2D energy profile.

Figure 16 - 3 MPa RFPA2D energy profile.

Graphics analysis allows identifying that there are similarities in the energy profiles of all simulations. The Figure 17 shows this similarity graph and highlights two trends:
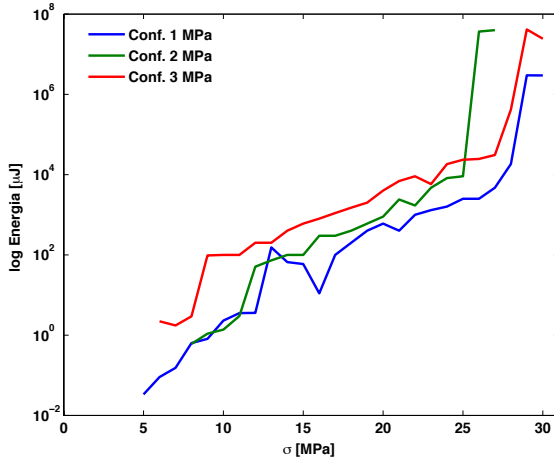

Figure 17 – RFPA Simulation energies profile.

Clearly, for the three containment tensions there are two steps of abrupt increase of the energy released by AE one at the beginning of the emission and another at failure. Among the steps all simulations appear to enter a level where the average increased energy is gradual and almost constant at around 700 µJ per MPa of increased pressure. Since these features common to all three can be in the presence of a simulation of the energy signature of the test. Furthermore, the emission power of the simulation to 2 MPa confinement are almost perfectly framed by the other, this being

particularly evident in Figure 18. This is indicative of the effect of confinement stress on energy breakage of the elements.
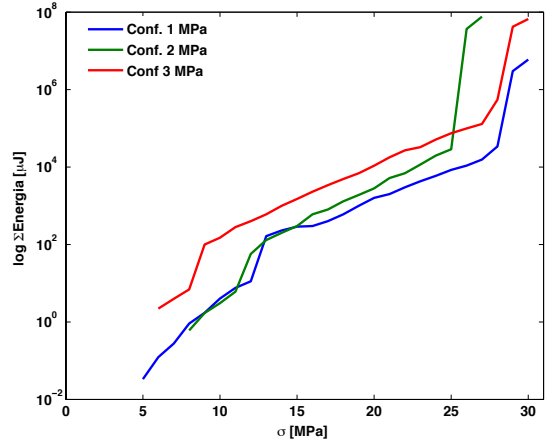

Figure 18 – RFPA accumulated energy profiles.

Note also that the higher the pressure containment voltage required for emission is initiated and acoustic lower the burst pressure of the sample events, i.e., a range of compression pressures that occur in the EA. In figure 19 where one can see the average contribution of each to total energy EA throughout the test, it is possible once again to verify that the confinement does indeed influence the energy levels of EA.
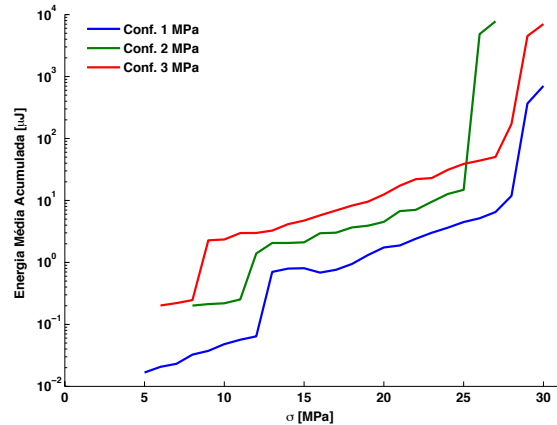

Figure 19 – Accumulated avarage energies (RFPA).

It is particularly evident that during the test the average energy released per EA grows exponentially. Figure 19 also shows that the ratio of the growth is enhanced by the increased effective stresses.
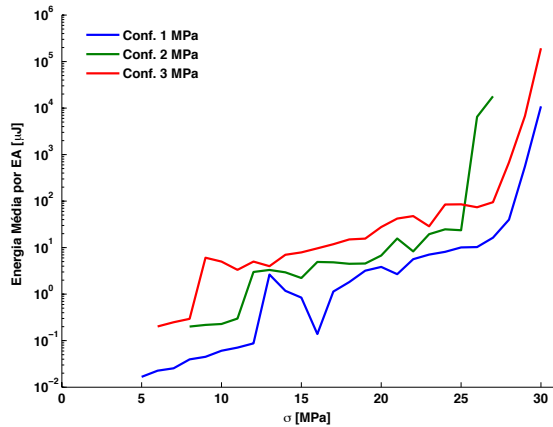
Figure 20- Average AE energy (RFPA).

The graph of Figure 47 compared with previous data shows that although the number of events falling dramatically post break the energy released is virtually identical to the releasing failure.

LABORATORY ENERGETIC PROFILES

The energy profiles of representative assays of 1 MPa (PV 27) 2 MPa (PV28) and 3 MPa (PV34c) shown in Figures 21, 21 and 23, respectively, would see that there is indeed a discrepancy between the results of simulation and laboratory results.
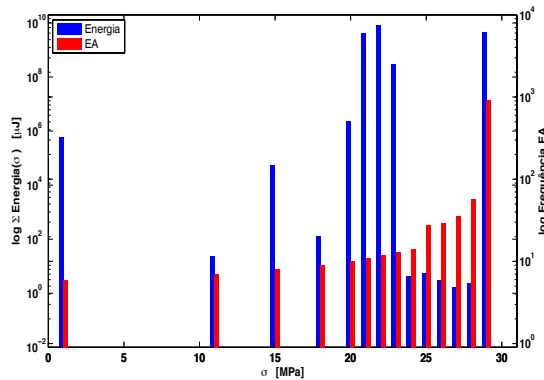

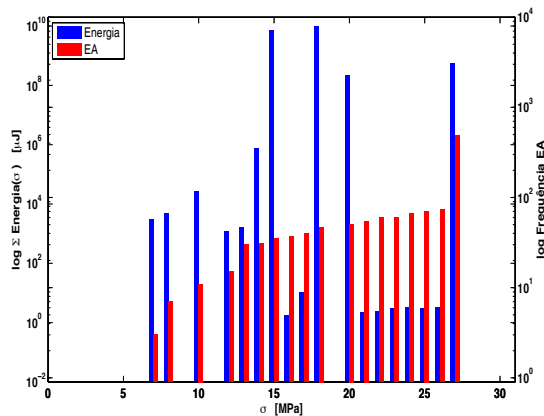Figure 21 – Energy profile for 1 MPa confined PV27.

Figure 22 - Energy profile for 2 MPa confined PV28.

In fact although it is possible to find slight similarities in terms of the AE profiles, in particular the constant monotony for the containment of tensions 1 and 2 MPa, these end here.

Laboratory energy profiles have very different behaviours of their simulations RFPA. From already clear discontinuity along the load increase while in the simulations is the development of arrhythmias continues throughout the simulation. On the other hand the variability of monotony that is extremely complex in the energy profiles of laboratory tests and which has no expression on the results of simulations RFPA. Finally the range of energies emitted. Although in both cases the amount of detected event is of the order of thousands of events, laboratory thousands to tens of thousands RFPA, the energy released in the laboratory tests is the order of 10^9 µJ whereas in simulation the accumulated values are of the order of 10^7 µJ.
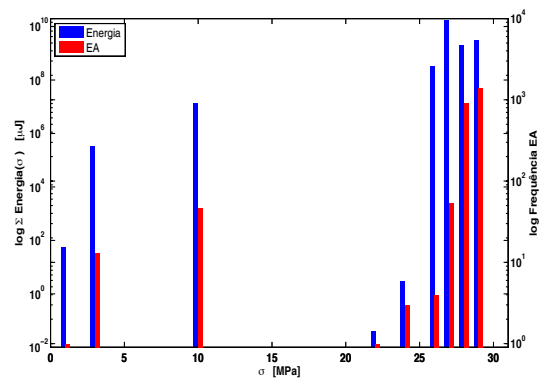

Figure 23 - Energy profile for 3 MPa confined PV34c.

Figure 24 highlights the profiles of the average energy delivered by acoustic event detected during the tests. Note that the three tests show four power peaks, which in all cases only coincide with peak emissions in the bursting pressure. Note also that there is a similarity with the RFPA simulations in that also in laboratory assays were 2 MPa which have demonstrated the lowest range of AE activity.
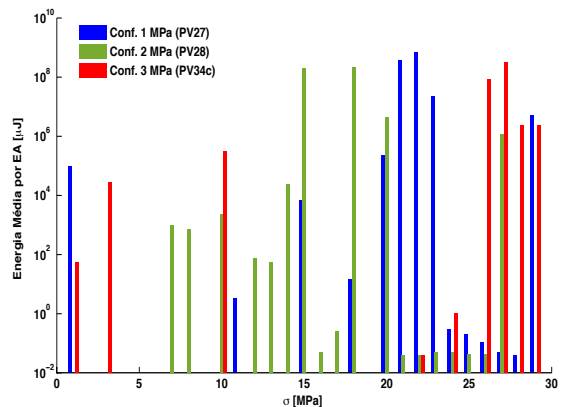

Figure 24 – Average AE energy profiles (Laboratório).

Note also that after each peak energy emissions that follow are particularly weak, even more generally. To try to understand the origin of this behavior of the energy profiles of laboratory tests explores in more detail the energy distribution of the EA. This distribution is represented by a bivariate histogram of the energy along the increased internal radial stress and is shown in Figures 25, 26 and 27 for the reference tests 1, 2 and 3 MPa confinement respectively.
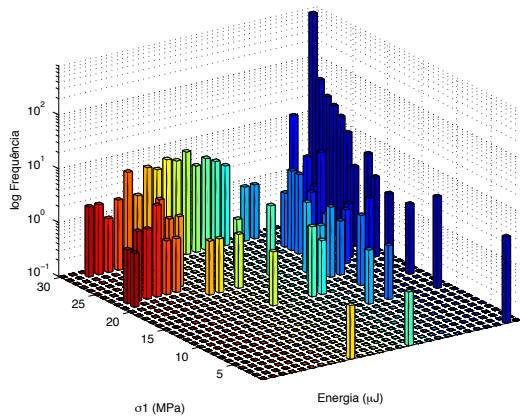
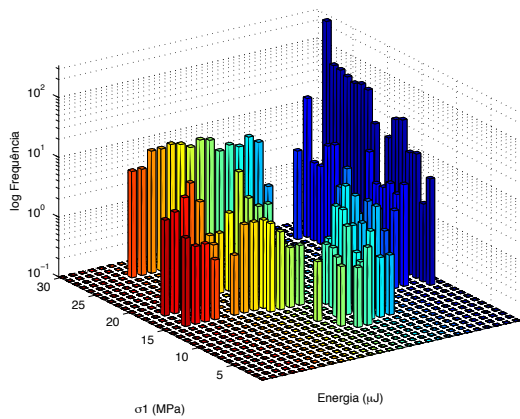Figure 25 – Energy distribution for 1 MPa confined PV27.

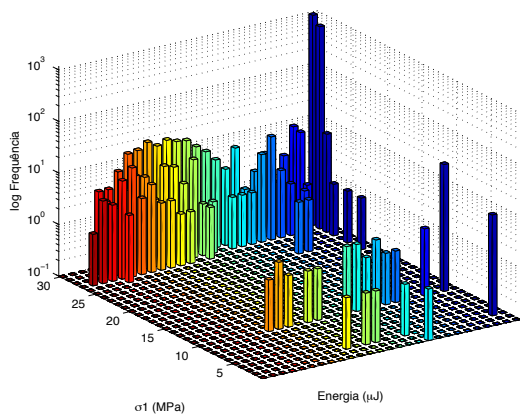Figure 26 – Energy distribution for 2 MPa confined PV28.

Figure 27 – Energy distribution for 3 MPa confined PV34c.

They are making several enlightening trends. The first is that as the load is increased during the trial not only the frequency of the highest energy events increases, but also the energies of these events increases. Moreover it is noted that analyzing all the test and following the same along the axis of the energies can be noted around the EA detection of

discontinuities these discontinuities increase the effect of the increase and decrease of energy in the opposite direction. Another finding is the clear existence of an energy signature repeated failure in all tests confirming the trend observed in the simulations.

FINDINGS

Conclusions can be drawn from both the dimensions that this work proposed to investigate. First regarding the location of acoustic events with complex geometry:

We conclude that the developed methodology to locate the source of acoustic emissions from laboratory tests on hollow cylinders produces results with good agreement with the visual analysis. Errors obtained in the location are acceptable, considering the error inherent to the sensors. Consequently it follows that the methodology performance improvement with the use of smaller sensors.

It follows also, as regards to the quantity of AE located, that the methodology would benefit considerably from implementing a frequency low-pass filter in the amplifier in conjunction with a high-pass filter in the drive or already programmed into the software. This would eliminate the two identified components of noise and therefore would increase the detection events as well as the location/detection rate. The produced locations allow good indications of the areas with the highest incidence of AE and approach the direction of the final fracture profile.

Also the location algorithm appears to improve efficiency by increasing the magnitude of confinement stress.

As for fracturing, it was concluded that the manner of rupture is essentially determined by the geometry of the test and the characteristics of the rock matrix and it's micro fracturing. In fact for the three tested confinement conditions the final profile of rupture is very similar, so the magnitude of the applied confinement stresses appears to have no influence on the shape of the rupture.

Moreover the energy distribution of the portions leading to the fracturing ruptures has a greater dependence on the magnitude of the effective stresses than pre-existing micro fracturing. It was also observed that the probability of an event being detected, to be located is a function of both rock matrix and the boundary conditions of the test, the weight being however greater dependence of the latter. This explains why increasing the magnitude of the containment increase the efficiency of the locating algorithm.

As the capacity of the RFPA rock breaking simulation software to simulate the ECO it is concluded that the performance is not satisfactory. Having been the intention of the authors to simulate the variability of the mechanical properties of the rock, how this variability is introduced impossible to obtain consistent results. In fact the software is able to simulate the rupture profile observed in the laboratory, but the probability of making a set of independent and simulations with the same settings is about 5%. However by comparing the simulations and laboratory findings it is concluded that the variability of the mechanical properties of the rock matrix is strongly anisotropic, so that the implementation of such a parameter for defining the anisotropy RFPA algorithm would greatly benefit from their performance.

The simulation RFPA was however able to simulate an apparent energy signature of the test, which are seen sharp increases in the average energy released by EA. This behaviour was indeed observed, although with more

complex profiles, in laboratory tests. There are clearly in each test, 4 cargo areas where it is found that the average energy by EA increases abruptly, and then again decrease.

The loads that these phenomena occur vary from test to test regardless of confinement. It was concluded that the rock matrix and its pre-existing micro fracturing essentially determine the distribution of this behaviour. So it may be a way to assess the heterogeneity of the mechanical properties of the rock matrix.

The nature of this phenomenon could have the following explanation: Since the ECO is held in a hollow cylinder increasing triaxial confinement promotes deformation of the material along the external and internal surfaces of the sample. Thus, part of the energy that otherwise would be released as a detectable AE is spent on deformation of the material. The acoustic events resulting from these bursts have lower energies than those occurring within the interior of the specimen, so the probability of the event being detected decreases with increasing load.

On the other hand the deformation of these elements promote the concentration of tensions elements inside the specimen with higher resistance. These in turn breaking with increasing strain emit AE with high energy and force rapid strain redistribution into the surrounding tension elements, It is thus explaining the reason why the average energy of AE decreases after each sudden increase.

BIBLIOGRAPHY

AZO Materials. (2013). AISI A514 Grade B Alloy Steel (UNS K11630). Retrieved from http://www.azom.com/article.aspx?ArticleID=6737

Baxter, M. G., Pullin, R., Holford, K. M., & Evans, S. L. (2007). Delta T source location for acoustic emission. *Mechanical Systems and Signal Processing*, *21*(3), 1512–1520. doi:10.1016/j.ymssp.2006.05.003

European Commission. (2011). Europe 2020 – Europe's growth strategy. *Europa Website - Europe 2020*. doi:10.1016/j.resconrec.2010.03.010

Grabec, I., & Sachse, W. (1989). Application of an intelligent signal processing system to acoustic emission analysis. *Journal of the Acoustical Society of America*, *85*(3), 1226–1235.

Grosse, C. U., & Ohtsu, M. (Eds.). (2008). *Acoustic Emission Testing: Basics for Research - Applications in Civil Engineering [Hardcover]*. Springer; 2008 edition. Retrieved from http://www.amazon.co.uk/Acoustic-Emission-Testing-Applications-Engineering/dp/3540698957

Hagan, M. T., Demuth, H. B., & Beale, M. H. (1996). *Neural network design. Boston Massachusetts PWS* (Vol. 2). Retrieved from http://ecee.colorado.edu/academics/schedules/ECEN5120.pdf

Hagan, M. T., & Menhaj, M. B. (1994). Training feedforward networks with the Marquardt algorithm. *IEEE Transactions on Neural Networks*, *5*(6), 989–993. doi:10.1109/72.329697

Hardy, H. R. J. (2005). *Acoustic Emission/Microseismic Activity: Volume 1: Principles, Techniques and Geotechnical Applications, Volume 1*. Retrieved from http://books.google.pt/books/about/Acoustic_Emission_Microseismic_Activity.html?id=Bt50nfeLFFcC&pgis=1

Hensman, J., Mills, R., Pierce, S. G., Worden, K., & Eaton, M. (2010). Locating acoustic emission sources in complex structures using Gaussian processes. *Mechanical Systems and Signal Processing*, *24*(1), 211–223. doi:10.1016/j.ymssp.2009.05.018

Hsu, N. N. (1977). Acoustic Emissions Simulator. US Patent.

Ing, R. K., Quieffin, N., Catheline, S., & Fink, M. (2005). In solid localization of finger impacts using acoustic time-reversal process. *Applied Physics Letters*, *87*(20).

King, G. E. (2012). Hydraulic Fracturing 101: What Every Representative, Environmentalist, Regulator, Reporter, Investor, University Researcher, Neighbor and Engineer Should Know About Estimating Frac Risk and Improving Frac Performance in Unconventional Gas and Oil Wells. In *SPE Hydraulic Fracturing Technology Conference*.

Kosel, T., Grabec, I., & Muzic, P. (2000). Location of acoustic emission sources generated by air flow. *Ultrasonics*, *38*(1–8), 824–826.

Kundu, T. (2014). Acoustic source localization. *Ultrasonics*, *54*(1), 25–38. doi:10.1016/j.ultras.2013.06.009

Marquardt, D. W. (1963). An Algorithm for Least-Squares Estimation of Nonlinear Parameters. *Journal of the Society for Industrial and Applied Mathematics*. doi:10.1137/0111030

Melikoglu, M. (2014). Shale gas: Analysis of its role in the global energy market. *Renewable and Sustainable Energy Reviews*, *37*, 460–468. doi:10.1016/j.rser.2014.05.002

Mobley, K. et al. (1987). Survey of Commercial Sensors and Systems for Acoustic Emission Testing. In P. M. McIntire (Ed.), *Nondestructive Testing Handbook Vol:5* (pp. 513–549). Columbus, Ohio: American Society for Nondestructive Testing.

Park, B., Sohn, H., Olson, S. E., DeSimio, M. P., Brown, K. S., & Derriso, M. M. (2012). Impact localization in complex structures using laser based time reversal. *Structural Health Monitoring: An International Journal*, *11*(5), 57–588.

Ribay, G., Catheline, S., Clorennec, D., Ing, R. K., Quieffin, N., & Fink, M. (2007). Acoustic Impact Localization in Plates: Properties and Stability to Temperature Variation. *IEEE TRANSACTIONS ON ULTRASONICS FERROELECTRICS AND FREQUENCY CONTROL*, *54*(2), 378–385.

SAUSE, M. G. R. (2011). INVESTIGATION OF PENCIL-LEAD BREAKS AS ACOUSTIC EMISSION SOURCES. *Journal of AE*, *29*, 184–196.

Scruby, C. ., & Drain, L. . (1990). *Laser Ultrasonics Techniques and Applications*. New York: Taylor & Francis. Retrieved from http://books.google.pt/books/about/Laser_Ultrasonics_Techniques_and_Applica.html?id=KgXPqx9ST-wC&pgis=1

Sribar, R., & Sachse, W. (1993). An experimental investigation of the AE source location and magnitude on 2-D frame structures using intelligent signal processing. *Journal of the Acoustical Society of America*, *93*(4).

Staszewski, W. J., Lee, B. C., Mallet, L., & Scarpa, F. (2004). Structural health monitoring using scanning laser vibrometry: Part 1 - Lamb wave sensing. *Smart Materials and Structures*, *14*(2), 251–260.

WETTMANN, R. W. (2011). *GERMANY'S WITHDRAWAL FROM NUCLEAR ENERGY*. London.

World Nuclear Association. (2014). Fukushima Accident. Retrieved July 7, 2014, from http://www.world-nuclear.org/info/safety-and-security/safety-of-plants/fukushima-accident/